

1       **Use of bender elements to evaluate linkages between thermal volume changes and shear**  
2                   **modulus hardening in drained and undrained thermal triaxial tests**

3

4                   **Radhavi A. Samarakoon, Ph.D.**

5       Graduate Research Assistant, Department of Structural Engineering, University of California San  
6                   Diego, La Jolla, CA 92093-0085, USA; Email: rabeysir@eng.ucsd.edu

7

8                   **Isaac L. Kreitzer, B.S.**

9       Graduate Research Assistant, Department of Structural Engineering, University of California San  
10                  Diego, La Jolla, CA 92093-0085, USA; Email: ikreitzer@ucsd.edu

11

12                  **John S. McCartney, Ph.D., P.E., F.ASCE (Corresponding Author)**

13       Professor, Department of Structural Engineering, University of California San Diego, La Jolla, CA  
14                  92093-0085, USA; Email: mccartney@ucsd.edu

15

16 **Abstract** This study investigates linkages between volume change, pore fluid drainage, shear  
17 wave velocity, and temperature of soft clays using a thermal triaxial cell equipped with bender  
18 elements, a measurement approach that has not been explored widely in past thermo-  
19 mechanical studies. Two kaolinite specimens were consolidated mechanically to a normally  
20 consolidated state and then subjected to drained and undrained heating-cooling cycles,  
21 respectively. After cooling the specimens were subjected to further mechanical consolidation to  
22 evaluate changes in apparent preconsolidation stress. Both specimens showed net contractive  
23 thermal strains after a heating-cooling cycle and overconsolidated behavior during mechanical  
24 compression immediately after cooling. The shear wave velocity increased during drained  
25 heating but negligible changes were observed during drained cooling, indicating permanent  
26 hardening due to thermal consolidation during the heating-cooling cycle. The shear wave velocity  
27 decreased during undrained heating due to a reduction in effective stress associated with  
28 thermal pressurization of the pore fluid, but subsequently increased when drainage was  
29 permitted at elevated temperature. The shear wave velocity increased slightly during undrained  
30 cooling but decreased when drainage was permitted at room temperature. Net increases in  
31 small-strain shear modulus of 17 and 11% after heating-cooling cycles under drained and  
32 undrained (with drainage after reaching stable temperatures) conditions, respectively, provide  
33 further evidence to the potential of thermal soil improvement of normally consolidated clays.  
34 Transient changes in shear modulus also highlight the importance of considering drainage  
35 conditions and corresponding changes in effective stress state during heating-cooling cycles.  
36 **Keywords:** thermal volume change, shear wave velocity, shear modulus, bender elements,  
37 thermal triaxial cell, normally consolidated clay

38     **1. Introduction**

39     The impact of temperature on the behavior of clay is important to understand in many  
40     geotechnical engineering applications but is particularly critical in in-situ heating for soil  
41     improvement, also referred to as thermal soil improvement. Thermal soil improvement has been  
42     investigated to improve soft clay layers using thermal drains or energy piles (e.g., Abuel-Naga et  
43     al. 2006, Pothiraksanon et al. 2010; Samarakoon and McCartney 2020a, 2021; Ghaaowd and  
44     McCartney 2021; Ghaaowd et al. 2022). Thermal drains are vertical porous drains (sands or  
45     geosynthetic) that include a geothermal heat exchanger and improve soils by providing both a  
46     constant temperature and a free drainage boundary condition for thermal consolidation  
47     (Samarakoon and McCartney 2022). Energy piles are rigid elements that provide structural  
48     support and heat exchange capabilities, and the heat exchange process can be used to enhance  
49     the pullout capacity (Ghahaowd et al. 2022). Despite the development of these thermal soil  
50     improvement techniques, the mechanisms of thermal soil improvement are still not well  
51     understood, including coupled effects of pore fluid pressurization, effective stress changes, shear  
52     modulus changes, and volume changes. Accordingly, the objective of this study is to evaluate the  
53     impact of drainage conditions and thermo-mechanical loading paths on the thermal volume  
54     change and the corresponding changes in the shear modulus of the soil, as well as to evaluate  
55     the coupling between thermal pressurization of pore water during undrained heating or cooling,  
56     pore water dissipation during drained heating or cooling, and volume change in saturated  
57     normally consolidated clay specimens. Further, this study seeks to better understand the  
58     transient trends in the important variables during a thermo-mechanical loading path as many  
59     previous studies only focused on equilibrium conditions. Information on the transient linkages

60 between thermo-mechanical loading paths and soil shear modulus will be useful when  
61 determining design parameters in a thermal soil improvement application as well as in the design  
62 of energy geostructures.

63 Several researchers have investigated the effect of temperature on soil behavior including  
64 volume change, shear strength, stiffness, and hydraulic conductivity. Many of these studies were  
65 focused on highly overconsolidated clays. General observations were that volumetric strains  
66 during drained heating are expansive and elastic for overconsolidated clays, and that the  
67 magnitude of thermoelastic volumetric strains is dependent on the effective stress and the  
68 overconsolidation ratio (Baldi et al. 1988; Hueckel and Baldi 1990; Abuel-Naga et al. 2007a). On  
69 the other hand, fewer studies have focused on normally consolidated clays. General observations  
70 are that drained heating results in plastic contractive volumetric strains whereas undrained  
71 heating results in elastic expansion (Hueckel and Baldi 1990; Cekerevac and Laloui 2004; Abuel-  
72 Naga et al. 2007a; Uchaipichat and Khalili 2009). The contractile thermal volumetric strains  
73 observed during drained heating of normally consolidated clays also leads to an increase in  
74 undrained shear strength (Houston et al. 1985; Kuntiwattanakul et al. 1995; Abuel-Naga et al.  
75 2006; Samarakoon et al. 2018, 2022).

76 The drained shear strength was also observed to increase with temperature as a result of the  
77 soil being subjected to a temperature history (Cekerevac and Laloui 2004; Abuel-Naga et al.  
78 2007b). Alsherif and McCartney (2015) noted that temperature effects on the shear strength of  
79 soils also indirectly affects the secant Young's modulus in the axial strain range of 1-3%. The  
80 small-strain shear modulus, typically corresponding to shear strains less than 0.001%, is an  
81 important parameter needed for characterizing the elastic soil behavior related to geotechnical

82 structures such as foundations, tunnels, pavements, deep excavations, and the soil response  
83 during earthquakes (Atkinson and Sallfors 1991; Mair 1993; Ishihara 1996; Atkinson 2000). At  
84 very small strains, the stress-strain behavior of soil is linear elastic with constant shear modulus  
85 whereas at higher strains, the soil behavior is observed to be non-linear with reductions in shear  
86 modulus with increasing strain (Atkinson 2000). The small-strain shear modulus represents the  
87 mechanical response of a soil in its intact state and depends on factors such as void ratio,  
88 confining stress, and apparent preconsolidation stress (Hardin and Black 1969; Khosravi and  
89 McCartney 2012). In geotechnical engineering applications including the use of in-situ heating for  
90 soil improvement (Abuel-Naga et al. 2006, Pothiraksanon et al. 2010; Samarakoon and  
91 McCartney 2020a, 2021) as well as energy geostructures such as energy foundations and soil  
92 borehole thermal energy storage systems (Brandl 2006, Laloui et al. 2006, Stewart et al. 2014,  
93 Murphy et al. 2015), it is expected that the void ratio, effective stress, and apparent  
94 preconsolidation stress may change, which indicates that the small-strain shear modulus may be  
95 a good indicator of the effects of these parameters which may be difficult to measure directly  
96 (i.e., the apparent preconsolidation stress). Most existing thermo-mechanical constitutive  
97 models assume that the elastic moduli of soil are independent of temperature (Hueckel and  
98 Borsetto 1990; Cui et al. 2000; Laloui and Cekerevac 2003). However, considering the effect of  
99 temperature on these parameters will allow for better predictions when designing geotechnical  
100 structures subjected to temperature fluctuations. Furthermore, geotechnical structures such as  
101 pavements and other earthen structures are also subjected to fluctuations in temperature due  
102 to climate effects (McCartney and Khosravi 2013; Vahedifard et al. 2020), so an understanding of  
103 the effects of temperature on the small-strain shear modulus may be useful in these applications.

104 A limited number of studies have been conducted on the effect of temperature on the elastic  
105 moduli of soil (Young's modulus or shear modulus) defined at strains less than 0.001%. The effect  
106 of temperature and thermal cycles on the small-strain shear modulus of saturated lateritic clay  
107 were investigated by Bentil and Zhou (2022) using a temperature-controlled oedometer setup  
108 equipped with bender elements. It was observed that for a given vertical effective stress, the  
109 small-strain shear modulus at 40 °C was lower compared to its value at 5 °C. However, the small-  
110 strain shear modulus was found to increase by about 16% for normally consolidated specimens  
111 after being subjected to four thermal cycles ranging from 5 – 40 °C. Other have studied the effects  
112 of temperature on the secant Young's modulus of soils at higher strains, which can be related to  
113 the secant shear modulus via the Poisson's ratio. Kuntiwattanakul et al. (1995) and Cekerevac  
114 and Laloui (2004) used triaxial tests to investigate the effects of temperature on the secant  
115 Young's modulus of Kaolin clay at larger strains. The secant shear modulus was obtained at a  
116 strain of 0.1% in the study by Kuntiwattanakul et al. (1995) for a temperature range of 0 – 90 °C  
117 whereas Cekerevac and Laloui (2004) determined the secant Young's modulus for an axial strain  
118 of 0.5% at temperatures ranging from 22 – 90 °C. In both studies, the secant Young's modulus  
119 was found to increase with increasing temperature. Similar observations were made by Abuel-  
120 Naga et al. (2006) for Bangkok clay where the secant modulus was measured at different  
121 deviatoric stress ratios corresponding to axial strains between 0.01% and 6%.

122 The discrepancies observed in the limited data on soil stiffness parameters may arise due to  
123 the differences in the stress or strain states, temperatures and drainage conditions used in the  
124 studies. For instance, at higher temperatures, the thermal volume change and its effects on soil  
125 stiffness can be more significant. On the other hand, heating and shearing under undrained

126 conditions will lead to generation of excess pore water pressure, reducing the effective stress of  
127 the clay which in turn will decrease the shear modulus. Furthermore, measuring the secant  
128 modulus at higher strain levels may incorporate thermo-plasticity effects and soil fabric changes.  
129 In addition, the elastic moduli of soil may also be dependent on the mechanical and thermal  
130 loading paths. For example, Bentil and Zhou (2022) saw a difference of about 8% in the small-  
131 strain shear modulus of a saturated lateritic clay specimen subjected to a compression-cooling  
132 path vs. a cooling-compression path. Vahedifard et al. (2020) found a negligible change in small-  
133 strain shear modulus of a saturated, compacted silt with an increase in temperature of 20 °C but  
134 found decreases in small-strain shear modulus during heating of unsaturated, compacted silt  
135 with increasing suction. In view of the limited studies available in literature and the  
136 inconsistencies observed in reported data, further investigation is required to better understand  
137 the effects of temperature on the small-strain elastic moduli of normally consolidated clay. To  
138 that end, this study focuses on the effect of a heating-cooling cycle on the volume change and  
139 small strain shear modulus of normally consolidated clay using drained and undrained thermal  
140 triaxial tests in a cell that incorporates bender elements into the top and bottom platens.

141 Bender elements are widely used in laboratory testing to measure shear wave velocity in soils  
142 and have been integrated into many standard geotechnical laboratory testing devices including  
143 triaxial and oedometer cells (Shirley and Hampton 1978; Dyvik and Madshus 1985; Fam and  
144 Santamarina 1995; Viggiani and Atkinson 1995; Pennington et al. 2001; Ghayoomi and McCartney  
145 2011). Bender elements are piezoelectric bending actuators which can convert electrical energy  
146 to mechanical energy and vice versa. The transmitting element is excited with a small voltage  
147 where it generates a bending motion to induce a vertically propagating shear wave (or s-wave)

148 in a soil layer. The vibration propagating through the soil is detected by the receiver element that  
149 outputs a voltage signal. The transmitted and the received waveforms can be used to obtain the  
150 shear wave velocity. The shear wave velocity ( $V_s$ ) is calculated using the time required for the  
151 wave to travel from the transmitter to the receiver and the tip-to-tip distance between benders:

152 
$$V_s = \frac{\text{tip-to-tip distance}}{\text{travel time}} \quad (1)$$

153 The small strain shear modulus ( $G_0$ ) can be obtained using the following relationship where  $\rho$   
154 is the total density of the soil (Hardin and Blandford 1989):

155 
$$G_0 = \rho V_s^2 \quad (2)$$

156 The total density of the soil can be estimated using the following relationship:

157 
$$\rho = \frac{(G_s + S e) \rho_w}{1 + e} \quad (3)$$

158 where  $G_s$  is the specific gravity of the soil,  $S$  is the degree of saturation (equal to 1 for the  
159 saturated clay in this study),  $e$  is the void ratio, and  $\rho_w$  is the density of water. The form of  
160 Equation (2) indicates that changes in total density of the soil due to thermal volume changes  
161 (i.e., changes in void ratio) may affect the value of  $G_0$  calculated from the value of  $V_s$  in addition  
162 to the changes in tip-to-tip distance associated with the calculation of the value of  $V_s$ .  
163 Accordingly, thermal volume change and  $G_0$  should be closely linked. The density of water in  
164 Equation (3) varies with temperature as follows (Hillel 1981):

165 
$$\rho_w = 1 - 7.37 \times (10^{-6}) \times (T - 4)^2 + 3.79 \times (10^{-8}) \times (T - 4)^3 \quad (4)$$

166 where  $\rho_w$  has units of  $\text{g}/\text{m}^3$  and  $T$  is in  $^{\circ}\text{C}$ . While the effects of temperature on  $\rho_w$  cancel out in  
167  $\rho_w G_s$  in the first term of the numerator in Equation (3), they are still present in the second term  
168 of the numerator in Equation (3) and should be included in the calculation of total density. It  
169 should be noted that the effects of temperature on the water density are more important in

170 drained conditions as the water entering or exiting the specimen may have a different density  
171 after temperature changes, while in undrained conditions the mass is constant and only the  
172 volume of the specimen changes.

173 Relationships for  $G_0$  such as those developed by Hardin and Black (1969) and Khosravi and  
174 McCartney (2012) indicate that  $G_0$  is not only sensitive to the void ratio but also to the effective  
175 stress state and preconsolidation stress. For example, these values follow the power law  
176 relationship of Hardin and Black (1966) expressed as follows, neglecting the effects of void ratio  
177 and overconsolidation ratio:

$$G_0 = AP_{atm} \left( \frac{\sigma'_{mean}}{P_{atm}} \right)^n \quad (5)$$

178 where  $\sigma'_{mean}$  is the mean effective normal stress,  $P_{atm}$  is the atmospheric pressure (101.3 kPa),  
179 and  $A$  and  $n$  are dimensionless fitting parameters. The presence of effective stress in Equation (5)  
180 indicates further possible linkages between  $G_0$  and thermal processes as it is well known that  
181 heating of saturated normally consolidated clays will lead to thermal pressurization which may  
182 change the effective stress state (Uchaipchat and Khalili 2009; Ghaoowd et al. 2017) and the  
183 apparent preconsolidation stress (Uchaipichat and Khalili 2009; Samarakoon and McCartney  
184 2020b). As noted, heating and cooling of clays will also result in changes in void ratio (Campanella  
185 and Mitchell 1968; Hueckel and Baldi 1990).

186 Compression wave velocities can be determined using uniaxial piezoelectric actuators in a  
187 similar manner to the shear wave velocities from bender elements, by imparting a vertically  
188 propagating compressive pulse on a soil layer. However, the compression wave velocity in  
189 saturated soils is typically not measured for saturated soils because the pore water has a higher  
190 compressive wave velocity than the soil skeleton (Valle-Molina and Stokoe 2012). Consequently,

191 the changes in compression wave velocity are not examined in this study. Materials tested,  
192 experimental procedures and the results of this study are discussed in the following sections.

193 **2. Material and Test Methods**

194 **2.1. Material**

195 This study was conducted on Kaolinite clay obtained from M&M Clays Inc. of McIntyre, GA.  
196 The properties of the clay are summarized in Table 1, including the compression indices obtained  
197 from an isotropic compression test at room temperature. The clay specimens evaluated in this  
198 study were prepared by mixing clay powder with deionized water in a commercial planetary  
199 mixer to form a slurry with a gravimetric water content of 115%. The slurry was then poured into  
200 a steel hollow cylinder of diameter 88.9 mm with porous stones and filter paper placed at the  
201 top and bottom. The slurry was first consolidated using a compression frame at a constant rate  
202 of 0.04mm/min for 48 hours. Then it was subjected to constant vertical stresses of 26, 52, 103  
203 and 181 kPa in 24 hour-long increments. The sedimented clay layer was extracted and trimmed  
204 to a smaller cylindrical specimen with a diameter of 72.4 mm and a height of 73 mm.

205 **2.2. Experimental Set-up**

206 A triaxial cell with a cell pressure capacity of 4 MPa and internal instrumentation obtained  
207 from GDS Instruments of Hook, UK was modified to perform temperature-controlled tests. The  
208 internal instrumentation includes a linearly variable differential transformer (LVDT) to measure  
209 the axial displacement of the specimen (suitable for pressures up to 3500 kPa and a temperature  
210 range of -20 to 110 °C), as well as piezoelectric bender elements embedded in the top and bottom  
211 caps to measure the compressional and shear wave velocities of the specimen. While the thermal  
212 triaxial system has an additional LVDT for measuring the radial displacement of the specimen,

213 this system could not be effectively mounted to the soft clay specimen, so only the axial  
214 deformation was measured, even though Samarakoon et al. (2022) noted that anisotropic  
215 thermal volume changes may occur in the clay. A pore water pressure transducer was used to  
216 monitor the changes in pore water pressure at the bottom of the specimen. Temperature control  
217 was achieved by circulating the cell fluid through a closed-loop copper heat exchanger that was  
218 embedded within a Julabo heat pump (model DYNEO DD-600F). The cell fluid was circulated using  
219 a high pressure, high temperature, circulating pump used in solar thermal panel applications  
220 (model S5 from US Solar Pumps). The closed-loop heat exchanger was connected to the top and  
221 bottom of the cell to mix the cell fluid and ensure uniform temperatures within the cell. The  
222 triaxial cell and the heat exchanger sections exposed to the environment were covered with  
223 insulation. The cell fluid temperature was measured using a thermocouple inserted at the top of  
224 the cell. It was assumed that the measured cell fluid temperature is representative of the  
225 specimen temperature. The cell and back pressures were controlled using a pressure panel. A  
226 picture and schematic of the thermal triaxial system are shown in Figure 1.

227 It is important to characterize the thermal deflections of the triaxial system during an  
228 application of temperatures as the mounts for the LVDT may expand and contract. Machine  
229 deflections due to temperature were obtained by using a dummy Aluminum specimen (linear  
230 thermal expansion coefficient,  $\alpha$  of  $2.3 \times 10^{-5}$  m/m°C) of height of 71.2 mm and diameter of  
231 71.11 mm. The aluminum dummy specimen had recesses around the bender elements for  
232 protection during the machine deflection tests. The machine deflections for the thermal triaxial  
233 system obtained from a test where a heating-cooling cycle was applied to the cell containing the  
234 aluminum dummy specimen with incremental temperature changes from 23 to 63 °C are shown

235 in Figure 2. The maximum temperature applied in the machine deflection test was the same as  
236 that used in the tests on soils. The machine deflections were calculated by subtracting the known  
237 elastic thermal deflections of the aluminum dummy specimen from the measured LVDT readings  
238 (raw displacement in Fig. 2). The machine deflections can then be used to correct the LVDT  
239 readings obtained in tests on soils.

240 **2.3. Procedure**

241 The trimmed clay specimen was placed atop the bottom pedestal of the thermal triaxial cell,  
242 carefully pushing the bender element in the base pedestal into the soft clay specimen to ensure  
243 intimate contact. The specimen was then encased within a Neoflex membrane from Karol  
244 Warner. The Neoflex membrane is made from pure latex coated with a layer of neoprene that  
245 can be used to temperatures up to 120 °C. The top cap was then carefully pushed into the top of  
246 the specimen, taking care that the bender element was aligned with the bottom bender element.  
247 After assembly of the internal LVDT and filling of the cell and heat exchange system with water,  
248 the specimen was back-pressure saturated by applying cell pressure and back-pressure in stages  
249 until the Skempton's pore water pressure parameter B value was at least 0.95. The specimen was  
250 then isotropically consolidated in stages to a mean effective stress of 250 kPa, which corresponds  
251 to normally-consolidated conditions. After mechanical consolidation, the specimen was  
252 subjected to a heating-cooling cycle, then compressed further to high stresses to measure any  
253 changes in mean apparent preconsolidation stress.

254 Two kaolinite specimens were tested in this study: one subjected to a drained heating-cooling  
255 cycle and the other subjected to an undrained heating-cooling cycle that included drainage stages  
256 after reaching a stable temperature after heating and after cooling, respectively. The purpose of

257 performing these tests is to evaluate the impact of drainage conditions on the thermal volume  
258 change of the soil, and to evaluate the coupling between thermal pressurization of pore water,  
259 pore water dissipation, and volume change in the specimens. Schematics of the thermo-  
260 mechanical paths for the drained and undrained tests are shown in Figures 3(a) and 3(b),  
261 respectively. Both specimens were first consolidated to normally-consolidated conditions (paths  
262 A-B and A'-B', respectively). For the specimen with drained heating (path B-C in Fig. 3(a)), the  
263 temperature was increased from 23 °C to 63 °C at a rate of 0.3 °C/hr that was sufficient to  
264 minimize the generation of thermally-induced excess pore water pressure within the specimen  
265 such that no change in mean effective stress occurs. After the temperature and axial displacement  
266 of the specimen were confirmed to be stable, the specimen was cooled back to room  
267 temperature (path C-D) at the same rate. Following this heating-cooling cycle, the specimen was  
268 isotropically compressed to a mean effective stress of 393 kPa (path D-E in Fig. 3(a)).

269 In the undrained heating-cooling test, drainage valves were closed during heating and cooling  
270 and the pore water pressure was measured at the base of the specimen. After stabilization of the  
271 pore water pressures during each stage of undrained heating and cooling, drainage was  
272 permitted only from the top of the specimen to track dissipation of thermally induced excess  
273 pore water pressure at the base. For the specimen with undrained heating (path B'-C' in Fig. 3(b)),  
274 the temperature was increased rapidly at a rate of 22 °C/hr to 63 °C from room temperature  
275 which was maintained until the thermally induced excess pore water pressure was observed to  
276 stabilize (approximately 80 hrs). The top drain valve was then opened to permit the specimen to  
277 drain after heating (path C'-D' in Fig. 3(b)). The specimen was then subjected to undrained cooling  
278 (path D'-E' in Fig. 3(b)) at the same rate as heating. The top drain valve was then opened again

279 to permit the specimen to drain after cooling (path E'-F'). Isotropic compression up to a mean  
280 effective stress of 393 kPa after a heating-cooling cycle is shown as path F'-G' in Figure 3(b).

281 The shear wave velocity was determined using bender elements following ASTM D8295-19 as  
282 closely as possible, and the shear modulus was calculated from the shear wave velocity and  
283 current value of total density using Equation (2). A deviation from the standard is that the  
284 specimen height/diameter ratio was 1:1 to facilitate reasonable times for the thermo-hydraulic  
285 processes, but different from typical applications of bender elements in triaxial cells, no shear  
286 stress was applied in the isotropic tests reported in this study. Shear wave velocity measurements  
287 were performed during each stage of testing and were analyzed using the GDS Bender Element  
288 Software. A sinusoidal wave with an amplitude of 14 V and excitation frequency 200 kHz was  
289 transmitted through the specimen. The arrival time was determined using the position of the first  
290 major peak of the received signal. The tip-to-tip distance at a given time was determined based  
291 on the initial height of the specimen and the axial displacement measured from the LVDT. Typical  
292 transmitted and received shear wave signals from the pair of bender elements in the triaxial cell  
293 are shown in Figure 4. Despite the short travel distance in the specimens, clean signals like those  
294 shown in Figure 4 were consistently obtained during the tests and no effect of temperature on  
295 the bender elements themselves was detected.

296 **3. Experimental Results**

297 **3.1. Typical Time Series Results**

298 Time series of axial strain and temperature during the heating-cooling cycles for the two  
299 specimens are shown in Figure 5, where compressive strains are defined as positive. The key  
300 transition points in these time series are labelled using the same notation as in Figure 3. The

301 mean effective stress in both specimens at the onset of the heating-cooling phase was  
302  $p'=250$  kPa. The results for the specimen experiencing a drained heating-cooling cycle are shown  
303 in Figure 5(a). The axial strain increases to 0.32% as the temperature increases followed by a  
304 slight decrease to 0.28% after drained cooling. The fact that thermal axial strains only occur  
305 during the applied changes in temperature confirms that the rate of heating used in this test was  
306 sufficient for the soil to be fully drained during heating and cooling. The axial strain of 0.28% at  
307 the end of the drained heating-cooling cycle confirms permanent contraction of the soil. The  
308 results for the specimen experiencing an undrained heating-cooling cycle are shown in  
309 Figure 5(b). The axial strain is observed to decrease to -0.32% as the temperature increases,  
310 corresponding to undrained expansion. Once the specimen is allowed to drain at the elevated  
311 temperature the specimen contracts to an axial strain of 0.23%. This is slightly smaller than the  
312 axial strain observed in the test with drained heating. During undrained cooling, the specimen  
313 contracts further to an axial strain of 0.47%. Once the specimen is allowed to drain at room  
314 temperature, the specimen expands slightly to an axial strain of 0.39%. The thermal axial strain  
315 after an undrained heating-cooling cycle with drainage permitted after the heating and cooling  
316 stages is 0.39%, which is greater than that observed in the drained heating-cooling cycle. This  
317 difference is attributed to the effective stress in the specimen at the onset of drainage.

318 Time series of excess pore water pressure during the two tests are shown in Figure 6. The  
319 excess pore water pressure generated during the test on the specimen with a drained heating-  
320 cooling cycle is negligible with fluctuations between 1-2 kPa in Figure 6(a). During undrained  
321 heating a much larger thermally induced excess pore water pressure of 218 kPa is generated as  
322 observed in Figure 6(b), corresponding to a decrease in mean effective stress. After the specimen

323 is allowed to drain under elevated temperatures, these pore water pressures dissipate back to  
324 zero, corresponding to an increase in effective stress back to the original value. During undrained  
325 cooling the excess pore water pressures decrease to -102 kPa, corresponding to an increase in  
326 mean effective stress. After the specimen is allowed to drain at room temperature the excess  
327 pore water pressures dissipate again back to zero. The temperatures presented were measured  
328 using a thermocouple inserted at the top of the cell, and it is assumed that the cell fluid  
329 temperature is representative of the specimen temperature (i.e., it is assumed that the  
330 temperature is homogeneous throughout the specimen). However, the use of multiple  
331 thermocouples in future tests may provide a better estimate of the temperature distribution  
332 within the specimen and whether a temperature gradient exists within the specimen due to the  
333 high thermal conductivity of the metallic base pedestal.

334 The axial strains from Figure 5(b) and the excess pore water pressures from Figure 6(b) from  
335 the undrained heating-cooling test are shown in Figure 7 to demonstrate the linkage between  
336 these variables. This figure is included to confirm that when the temperature is increased or  
337 decreased rapidly in undrained conditions, both the axial strains and excess pore water pressures  
338 will take some time to stabilize. Uchaipichat and Khalili (2009) observed that during undrained  
339 heating, the thermal expansion and decrease in effective stress correspond to movement along  
340 a recompression line, but the results in this figure indicate that movement along this  
341 recompression line will be a time dependent process.

342 **3.2. Shear Wave Velocity Measurements**

343 The measured shear wave velocities and the corresponding thermal axial strains for the  
344 drained and undrained tests are shown in Figures 8(a) and 8(b), respectively. The key transition

345 points from Figure 3 are labelled in these figures next to the shear wave velocity values for  
346 simplicity. For the specimen subjected to a drained heating-cooling cycle, the shear wave velocity  
347 increases with temperature by 17 m/s and remained almost constant during cooling. This  
348 increase can be attributed to the plastic thermal strains observed in the clay specimen. The  
349 results for shear wave velocity and the thermal axial strain for the specimen subjected to an  
350 undrained heating-cooling cycle is shown in Figure 8(b). During undrained heating the shear wave  
351 velocity is observed to decrease with temperature by 96 m/s. However, during drainage at  
352 elevated temperature, the shear wave velocity increases again by 34 m/s. A slight increase in  
353 velocity is observed during undrained cooling which again is reduced during drainage after  
354 cooling. A net increase of about 12 m/s is observed after the heating-cooling cycle including the  
355 drainage stages after each heating and cooling stages. The differences in the initial shear wave  
356 velocity of the two specimens are attributed to the differences in the initial conditions of the  
357 sedimented specimens, which had slightly different initial void ratios. Despite this difference, the  
358 results from the long-duration tests on both specimens follow expectations from our current  
359 understanding of thermal volume change and thermal pressurization and provides useful insight  
360 into the differences in behavior expected for drained and undrained heating-cooling cycles which  
361 is an important aspect to be considered in the design of energy geostructures.

362 **4. Analysis**

363 **4.1. Thermal Strains**

364 The change in thermal axial strain with temperature is shown in Figure 9(a) for the drained  
365 test and in Figure 9(b) for the undrained test. The key transition points from Figure 3 are labelled  
366 in these figures. Compressive strains observed during drained heating and the slight elastic

367 expansion during cooling agree with the observations made in literature for normally  
368 consolidated clays (Hueckel and Baldi 1990; Cekerevac and Laloui 2004; Abuel-Naga et al. 2007a).  
369 The net change in axial strain after a drained heating-cooling cycle was 0.28% and was observed  
370 to be contractive. The specimen subjected to an undrained heating-cooling cycle also observed  
371 a net contraction of 0.39%, which was slightly greater than that obtained from a drained heating-  
372 cooling cycle. The dissipation of thermally induced excess pore water pressure during undrained  
373 heating and cooling may have contributed to the increase in the axial displacement observed.

374 The overall time series of axial strain and temperature for the specimen subjected to a  
375 drained heating-cooling cycle including the initial and final compression stages are shown in  
376 Figure 10(a) and the corresponding compression curve is shown in Figure 10(b). The key  
377 transition points from Figure 3(a) are labelled in these figures. The axial strain of the specimen  
378 after consolidation under an isotropic load of 250 kPa is 3.3% as shown in Figure 10(a). As a result  
379 of being subjected to drained heating, the axial strain of the specimen increases to 3.6% then  
380 reduces slightly to 3.5% after drained cooling. After further mechanical compression up to a  
381 mean effective stress of 393 kPa, the specimen experienced an axial strain of 4.4%.  
382 Overconsolidated behavior can be observed in the compression curve in Figure 10(b) as the  
383 specimen is subjected to mechanical compression after a heating-cooling cycle, although the  
384 specimen was at a normally consolidated state prior to heating. The specimen regains a normally  
385 consolidated state at a higher stress state upon further loading. This stress state can be  
386 approximated as 300 kPa although additional data points will provide a more accurate estimate.  
387 Nevertheless, this observation conforms the thermal hardening behavior observed in literature

388 (Hueckel and Borsetto 1990; Abuel-Naga et al. 2007a) where the yield surface expands after a  
389 heating-cooling cycle.

390 The overall time series of axial strain and temperature for the specimen subjected to a  
391 undrained heating-cooling cycle including the initial and final compression stages are shown in  
392 Figure 11(a) and the corresponding compression curve is shown in Figure 11(b). The key  
393 transition points from Figure 3(b) are included in these figures. The time series results of axial  
394 strain indicates that the specimen has an axial strain of 3.7% after isotropic consolidation under  
395 a mechanical load of 250 kPa. During undrained heating, the axial strain decreases to 3.4% then  
396 increases to 3.9% following drainage at elevated temperature. Undrained cooling leads to an  
397 increase in axial strain up to 4.2% but then is reduced to 4.1% after drainage at room  
398 temperature. The specimen had a final axial strain of 4.4% after being subjected to further  
399 mechanical compression up to 393 kPa. The corresponding compression curve is shown in Figure  
400 11(b). Consistent with the observations of Uchaipichat and Khalili (2009), elastic expansion along  
401 the recompression line is observed during undrained heating. Similar observations were made  
402 by Ghaaowd et al. (2017) during undrained heating of the same kaolinite clay. Upon further  
403 mechanical compression after cooling the observed results were similar to those of the specimen  
404 subjected to drained heating and cooling, where overconsolidated behavior is observed after  
405 cooling. Interestingly, the contraction during undrained cooling is observed to fall onto the same  
406 path of the compression curve where the specimen displayed overconsolidated behavior during  
407 mechanical compression after cooling. The effective stress is higher during this stage due to the  
408 negative excess pore water pressures generated during undrained cooling. However, once the

409 specimen was allowed to drain, the excess pore water pressures dissipated and the specimen  
410 regains its previous stress state.

411 The compression curves in terms of volumetric strain for the drained and undrained  
412 specimens are shown in Figures 12(a) and 12(b), respectively where the volumetric strain was  
413 calculated using the axial strain results. The key transition points from Figure 3 are labelled in  
414 these figures. Although radial strains are expected to be higher than axial strains because of the  
415 specimen preparation process (Samarakoon et al. 2022), a simplified approach assuming  
416 isotropic conditions was used to estimate the volumetric strain where the volumetric strain was  
417 assumed to be equal to 3 times the measured axial strain.

418 **4.2. Small Strain Shear Modulus Estimates**

419 Calculation of the variations in small-strain shear modulus from the measured shear wave  
420 velocity must include the impacts of thermal volume change on the total density. Accordingly,  
421 the variations in total density were calculated using Equation (3) by converting the volumetric  
422 strains in Figure 12 into void ratio and accounting for the impact of temperature on the water  
423 density using Equation (4). In drained conditions, the changes in volume of the specimen will be  
424 equal to the volume of water flowing in or out of the specimen as it is water saturated, but the  
425 water density will change with temperature. In undrained conditions, the mass of the specimen  
426 is constant while the volume of the specimen is measured directly. The calculated total densities  
427 for the drained and undrained specimens during the different stages of the test are shown in  
428 Figures 13(a) and 13(b), respectively. The key transition points from Figure 3 are included in these  
429 figures. The trends in total densities are similar to the trends in the axial strains shown in Figure 8,  
430 which implies that including the effect of temperature on the water density in the calculation of

431 the total density is negligible compared to the effect of thermal volume changes but can be  
432 considered for completeness.

433 The values of  $G_0$  were then calculated for the two specimens using the measured shear  
434 modulus and the estimated total density using Equation (2). The calculated changes in  $G_0$  and  
435 thermal volumetric strain with temperature for the drained heating-cooling test are shown in  
436 Figure 14(a), along with the key transition points from Figure 3(a) shown next to the transitions  
437 in  $G_0$ . Like the shear wave velocity, the shear strain modulus increases during drained heating but  
438 shows no significant change during drained cooling. The thermal volumetric strain after a drained  
439 heating-cooling cycle is 0.84% whereas the corresponding increase in small strain shear modulus  
440 is 14%. This increase can be attributed to the plastic thermal strains observed and the  
441 corresponding increase in density (0.4% increase after a heating-cooling cycle) in the clay  
442 specimen (Eq. (2)). Samarakoon et al. (2022) also observed an increase in undrained shear  
443 strength in specimens subjected to drained heating. The trends in Figure 14(a) are also similar to  
444 trends in  $G_0$  measured for an unsaturated silt during drying and wetting by Khosravi and  
445 McCartney (2012) indicating that the permanent change in  $G_0$  could be associated with both the  
446 thermal volume change and the change in apparent preconsolidation stress. The calculated  
447 values of  $G_0$  and the corresponding thermal volumetric strains for the specimen subjected to an  
448 undrained heating-cooling cycle are shown in Figure 14(b), along with the key transition points  
449 from Figure 3(b) shown next to the transitions in  $G_0$ . Trends like to those observed for shear wave  
450 velocity are observed where the small strain shear modulus decreases with temperature during  
451 undrained heating then increases during drainage at elevated temperature. An increase in  $G_0$  is  
452 observed during undrained cooling then decreases during drainage at room temperature. The

453 thermal volumetric strain after being subjected to an undrained heating-cooling cycle is 1.2% and  
454  $G_0$  is observed to increase by 9%. Key results from the two tests are summarized in Table 2.

455 As described previously, the small strain shear modulus is dependent on factors including  
456 void ratio, effective confining stress and the apparent preconsolidation stress. When subjected  
457 to a heating-cooling cycle, thermally induced changes occur in the clay specimen. In addition,  
458 these thermal changes will also depend on the drainage conditions used. In a saturated normally  
459 consolidated clay, as investigated in this study, plastic contractive volume changes attributed to  
460 the effects of a drained heating cooling cycle. This reduction in void ratio and the densification of  
461 the soil will lead to an increase in the small-strain shear modulus. On the other hand, during  
462 undrained heating, expansion is observed and the small-strain shear modulus decreases.  
463 However, this expansion is thermo-elastic and is recovered during drainage and subsequent  
464 cooling where the shear modulus is observed to increase correspondingly. Furthermore, the  
465 generation of excess pore water pressure during undrained heating will decrease the effective  
466 stress within the clay specimen. This decrease in effective stress will also contribute to the  
467 reduction in the small strain shear modulus according to Equation (5). This indicates the  
468 importance of the changes in effective stress due to thermal pressurization on the value of  $G_0$ , as  
469 the impacts of permanent thermal volume change and changes in apparent preconsolidation  
470 stress are not expected to occur until drainage is permitted. On the other hand, during undrained  
471 cooling, the negative pore water pressures generated increases the effective stress of the  
472 specimen. Accordingly, an increase can be observed in the small strain shear modulus. When  
473 drainage is permitted, the pore pressures dissipated and the shear modulus is seen to reduce.  
474 Under both drainage conditions, after being subjected to a heating-cooling cycle, an increase in

475 the apparent preconsolidation stress of the clay was observed in Figures 10 through 12. Due to  
476 thermal hardening of the clay, the elastic domain is expanded where the initially normally-  
477 consolidated specimen behaves as an overconsolidated specimen immediately after a heating-  
478 cooling cycle. This increase in the apparent preconsolidation stress is another contributing factor  
479 to the changes in the small-strain shear modulus observed.

480 As mentioned, the tests presented in this study are time consuming and complex. Although  
481 only two tests are considered in this paper, the data presented has value in understanding the  
482 impacts of drainage conditions on soil thermo-mechanical behavior. Further testing is needed to  
483 better understand the effect of different specimen conditions and to understand uncertainty.  
484 Based on the results of this study, some useful insights can be drawn with respect to the thermal  
485 volume change and pressurization behavior of clay and their linkages with stiffness  
486 characteristics. This information is beneficial in geotechnical applications involving thermal  
487 loading such as the use of in-situ heating for soil improvement. The experimental approach  
488 described herein has not been used to study the different mechanisms of soil behavior during  
489 heating-cooling cycles with different drainage conditions, and only a limited number of studies  
490 have been performed on the thermal effects on small-strain shear modulus. Further  
491 investigations considering different conditions (i.e., stress states, initial void ratios, temperature  
492 ranges, rate of heating, soil types, etc.) will help enhance the understanding of the thermal  
493 effects on small-strain shear modulus.

494 **5. Conclusion**

495 This study presents the results of an experimental investigation where the transient linkages  
496 between thermal volume change and small-strain shear modulus were evaluated for two

497 normally consolidated kaolinite specimens subjected to drained and undrained heating-cooling  
498 cycles, respectively. In the specimen undergoing a drained heating-cooling cycle, the rates of  
499 heating and cooling were sufficiently slow to minimize the generation of thermally induced  
500 excess pore water pressures. In the specimen undergoing undrained heating and cooling,  
501 drainage was permitted after reaching thermo-hydraulic equilibrium at the end of cooling. In  
502 both specimens, net contractive thermal strains were observed at the end of the heating-cooling  
503 cycle with slightly higher strains obtained for the specimen subjected to the undrained heating-  
504 cooling cycle. Upon further mechanical compression after cooling, both specimens exhibited  
505 overconsolidated behavior, even though the specimens were at a normally consolidated state  
506 prior to heating. The shear wave velocity was observed to increase with temperature during  
507 drained heating and remained constant during drained cooling, leading to a net increase in shear  
508 wave velocity after the heating-cooling cycle. On the other hand, shear wave velocity was  
509 observed to decrease dramatically during undrained heating due to the increase in thermally  
510 induced pore water pressure followed by an increase during drainage at elevated temperature.  
511 During undrained cooling, a slight increase in velocity was observed with a subsequent reduction  
512 during drainage after cooling, but still resulting in a net increase in shear wave velocity after the  
513 heating-cooling cycle. The changes in small strain shear modulus calculated using the change in  
514 volume of the specimens were also observed to follow a similar trend to that of shear wave  
515 velocity for the kaolinite specimens. A net increase in small-strain shear modulus was observed  
516 in specimens after a heating-cooling cycle which can be attributed to the contractive thermal  
517 volume changes and the thermal hardening associated with the increase in preconsolidation  
518 stress observed in normally consolidated clay. Overall, the methodology and experimental

519 approach presented in this study can be used to better understand the effects of thermal  
520 improvement of soft clays.

521 **Acknowledgements**

522 Funding from NSF grant CMMI 1941571 is appreciated. The opinions are those of the authors.

523 **References**

524 Abuel-Naga, H.M., Bergado, D.T., Chaiprakaikeow, S. (2006). "Innovative thermal technique for  
525 enhancing the performance of prefabricated vertical drain during the preloading process."  
526 *Geotextiles and Geomembranes*. 24, 359-370.

527 Abuel-Naga, H.M., Bergado, D.T., Bouazza, A., Ramana, G.V. (2007a). "Volume change behaviour  
528 of saturated clays under drained heating conditions: experimental results and constitutive  
529 modeling." *Canadian Geotechnical Journal*. 44, 942-956.

530 Abuel-Naga, H.M., Bergado, D.T., Bee, F.L. (2007b). "Effect of temperature on shear strength and  
531 yielding behavior of soft Bangkok clay." *Soils and Foundations*. 47(3), 423-436.

532 Alsherif, N.A., McCartney, J.S. (2015). "Thermal behaviour of unsaturated silt at high suction  
533 magnitudes." *Géotechnique*. 65(9), 703-716. DOI: 10.1680/geot./14.P.049.

534 Atkinson, J.H., Sallfors, G. (1991). "Experimental determination of soil properties." General  
535 Report to Session 1. *Proceedings of the 10<sup>th</sup> ECSMFE*. Florence. 3, 915-956.

536 Atkinson, J.H. (2000). "Non-linear soil stiffness in routine design." *Géotechnique*. 50(5), 487-508.

537 Baldi, G., Hueckel, T., Pellegrini, R. (1988). "Thermal volume changes of mineral-water system in  
538 low-porosity clay soils." *Canadian Geotechnical Journal*. 25, 807-825.

539 Bentil, O.T., Zhou, C. (2022). "Effects of temperature and thermal cycles on the elastic shear  
540 modulus of saturated clay." *Journal of Geotechnical and Geoenvironmental Engineering*.  
541 148(7), 06022006.

542 Brandl, H. (2006). "Energy foundations and other thermo-active ground structures."  
543 *Géotechnique*. 56(2), 81-122.

544 Campanella, R.G., Mitchell, J.K. (1968). "Influence of temperature variations on soil behavior."  
545 *Journal of the Soil Mechanics and Foundation Division. ASCE*. 94(3), 709-734.

546 Cekerevac, C., Laloui, L. (2004). "Experimental study of thermal effects on the mechanical  
547 behaviour of a clay." *International Journal for Numerical and Analytical Methods in  
548 Geomechanics*. 28, 209-228.

549 Cui, Y.J., Sultan, N., Delage, P. (2000). "A thermomechanical model for clays." *Canadian  
550 Geotechnical Journal*. 37(3), 607-620.

551 Dyvik, R., Madshus, C. (1985). "Lab measurements of  $G_{max}$  using bender elements." *Norwegian  
552 Geotechnical Institution Publication*. Report No. 161, Oslo.

553 Fam, M., Santamarina, C. (1995). "Study of geoprocesses with complementary mechanical and  
554 electromagnetic wave measurements in an oedometer." *Geotechnical Testing Journal*. 18(3),  
555 307-314.

556 Ghaaowd, I., Takai, A., Katsumi, T., McCartney, J.S. (2017). "Pore water pressure prediction for  
557 undrained heating of soils." *Environmental Geotechnics*. 4(2), 70-78.

558 Ghaaowd, I., McCartney, J.S., and Saboya, Jr., F. (2022). "Centrifuge modeling of temperature  
559 effects on the pullout capacity of torpedo piles in soft clay." *Soils and Rocks*. 45(1),  
560 e2022000822. DOI: 10.28927/SR.2022.000822.

561 Ghaaowd, I., McCartney, J.S. (2021). "Centrifuge modeling methodology for energy pile pullout  
562 from saturated soft clay." *ASTM Geotechnical Testing Journal*. 45(2), 332-354. DOI:  
563 10.1520/GTJ20210062.

564 Ghayoomi, M., McCartney, J.S. (2011). "Measurement of small-strain shear moduli of partially  
565 saturated sand during infiltration in a geotechnical centrifuge." *Geotechnical Testing Journal*.  
566 34(5), 1-11.

567 Hardin, B.O., Black, W.L. (1969). "Closure to vibration modulus of normally consolidated clays."  
568 *Journal of Soil Mechanics and Foundations Division. ASCE*. 95(6), 1531–1537.

569 Hardin, B.O., Blandford, G.E. (1989). "Elasticity of Particulate Materials." *Journal of Geotechnical  
570 Engineering*. 115(6), 788–805.

571 Hillel, D. (1980), *Fundamental of Soil Physics*, Academic, San Diego, Calif.

572 Houston, S.L., Houston, W.N., Williams, N.D. (1985). "Thermo-mechanical behavior of seafloor  
573 sediments." *Journal of Geotechnical Engineering*. 111(12), 1249-1263.

574 Hueckel, T., Baldi, M. (1990). "Thermoplasticity of saturated clays: Experimental constitutive  
575 study." *Journal of Geotechnical Engineering*. 116(12), 1778-1796.

576 Hueckel, T., Borsetto, M. (1990). "Thermoplasticity of saturated soils and shales: constitutive  
577 equations." *Journal of Geotechnical Engineering*. 116(12), 1765-1777.

578 Ishihara, K. (1996). *Soil behaviour in earthquake geotechnics*. Oxford University Press.

579 Khosravi, A., McCartney, J.S. (2012). "Impact of hydraulic hysteresis on the small-strain shear  
580 modulus of low plasticity soils." *Journal of Geotechnical and Geoenvironmental Engineering*.  
581 138(11), 1326–1333.

582 Kuntiwattanakul, P., Towhata, I., Ohishi, K., Seko, I. (1995). "Temperature effects on undrained  
583 shear characteristics of clay." *Soils and Foundation*. 35(1), 147-162.

584 Laloui, L., Cekerevac, C. (2003). "Thermo-plasticity of clays: an isotropic yield mechanism."  
585 *Computers and Geotechnics*. 30(8), 649-660.

586 Laloui, L., Nuth, M., Vulliet, L. (2006). "Experimental and numerical investigations of the  
587 behaviour of a heat exchanger pile." *International Journal for Numerical and Analytical  
588 Methods in Geomechanics*. 30(8), 763-781.

589 Mair, R.J. (1993). "Developments in geotechnical engineering research: applications to tunnels  
590 and deep excavations. Unwin Memorial Lecture 1992." *Proceedings of the Institution of Civil  
591 Engineers – Civil Engineering*. 97(1), 27-41.

592 McCartney, J.S., Khosravi, A. (2013). "Field monitoring system for suction and temperature  
593 profiles under pavements." *Journal of Performance of Constructed Facilities*. 27(6), 818-825.

594 Murphy, K.D., McCartney, J.S., Henry K.H. (2015). "Thermo-mechanical response tests on energy  
595 foundations with different heat exchanger configurations." *Acta Geotechnica*. 10(2), 179-195.

596 Pennington, D.S., Nash, D.F.T., Lings, M.L. (2001). "Horizontally mounted bender elements for  
597 measuring anisotropic shear moduli in triaxial clay specimens." *Geotechnical Testing Journal*.  
598 24(2), 133-144.

599 Pothiraksanon, C., Bergado, D.T., Abuel-Naga, H.M. (2010). "Full-scale embankment  
600 consolidation test using prefabricated vertical thermal drains." *Soils and Foundations*. 50(5),  
601 599-608.

602 Samarakoon, R.A., Ghaaowd, I., McCartney, J. S. (2018). "Impact of drained heating and cooling  
603 on undrained shear strength of normally consolidated clay." *Proc. 2<sup>nd</sup> International*  
604 *Symposium on Energy Geotechnics*. Lausanne. A. Ferrari, L. Laloui, eds., Vienna. 243-249.

605 Samarakoon, R.A., McCartney, J.S. (2020a). "Analysis of thermal drains in soft clay." *GeoAmericas*  
606 *2020. 4<sup>th</sup> PanAm Conference on Geosynthetics*. Rio de Janeiro, Brazil. Oct. 26-31. 1-9.

607 Samarakoon, R.A., McCartney, J.S. (2020b). "Effect of drained heating and cooling on the  
608 preconsolidation stress of saturated normally consolidated clays." *GeoCongress 2020*. GSP  
609 315. Minneapolis, MN. ASCE. Feb. 25-28. 620-629.

610 Samarakoon, R.A., McCartney, J.S. (2021). "Performance of prefabricated thermal drains in soft  
611 clay." *Geosynthetics Conference 2021*. Kansas City, MO, USA. Feb. 21-24. Nicks, J. and  
612 Beauregard, M., eds. IFAI, Roseville, MI. 1-12.

613 Samarakoon, R., McCartney, J.S. (2022). "Simulation of thermal drains using a new constitutive  
614 model for thermal volume change of normally consolidated clays." *Computers and*  
615 *Geotechnics*. 153, 105100.

616 Samarakoon, R.A., Kreitzer, I.L., McCartney, J.S. (2022). "Impact of initial effective stress on the  
617 thermo-mechanical behavior of normally consolidated clay." *Geomechanics for Energy and*  
618 *the Environment*. 32. 100407.

619 Shirley, D.J., Hampton, L.D. (1978). "Shear-wave measurements in laboratory sediments." *The*  
620 *Journal of the Acoustical Society of America*. 63(2), 607-613.

621 Stewart, M.A., McCartney, J.S. (2014). "Centrifuge modeling of soil-structure interaction in  
622 energy foundations." *Journal of Geotechnical and Geoenvironmental Engineering*. 140(4),  
623 04013044.

624 Uchaipichat, A., Khalili, N. (2009). "Experimental investigation of thermo-hydro-mechanical  
625 behaviour of an unsaturated silt." *Géotechnique*. 59(4), 339–353.

626 Vahedifard, F., Cao, T.D., Thota, S.K., Samarakoon, R.A., McCartney, J.S. (2020). "A temperature-  
627 dependent model for small-strain shear modulus of unsaturated soils." ASCE Journal of  
628 Geotechnical and Geoenvironmental Engineering. 146(12), 04020136.

629 Valle-Molina, C., Stokoe, K.H. (2012). "Seismic measurements in sand specimens with varying  
630 degrees of saturation using piezoelectric transducers." Canadian Geotechnical Journal 49 (6),  
631 671-685.

632 Viggiani, G., Atkinson, J.H. (1995). "Interpretation of bender element tests." *Géotechnique*. 45(1),  
633 149-154.

634 ASTM Standard D8295 – 19 (2019). "Determination of shear wave velocity and initial shear  
635 modulus in soil specimens using bender elements." ASTM International, West Conshohocken,  
636 PA. DOI: 10.1520/D8295-19.

637 **Table 1** Properties of Georgia kaolinite clay

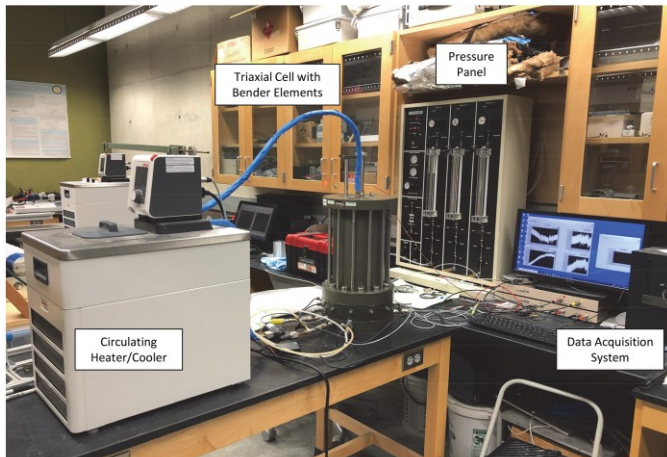
Parameter	Value
Liquid Limit	47
Plasticity Index	19
Specific Gravity	2.6
Slope of VCL ( $\lambda$ )	0.09
Slope of RCL ( $\kappa$ )	0.02
USCS Classification	CL

638

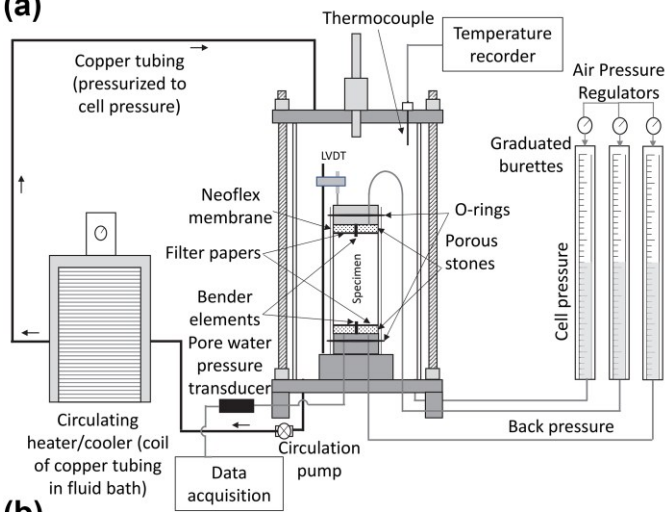
639 **Table 2** Summary of results

Parameter	Drained heating- cooling cycle	Undrained heating- cooling cycle
Initial void ratio	1.03	1.1
Initial total density (kg/m <sup>3</sup> )	1788	1755
Thermal axial strain after a heating-cooling cycle (%)	0.28	0.39
$V_s$ before heating (m/s)	255.9	312.7
$V_s$ after a heating-cooling cycle (m/s)	272.8	325.9
$G_0$ before heating (MPa)	122.7	180.8
$G_0$ after a heating-cooling cycle (MPa)	140.1	197.6
Final void ratio	0.84	0.82

640



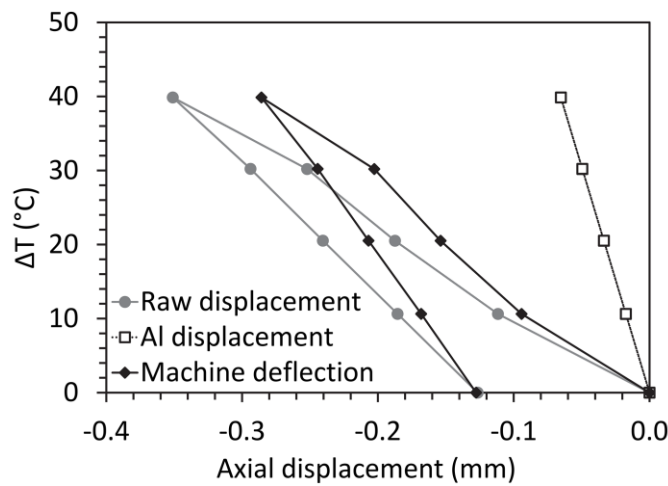
(a)



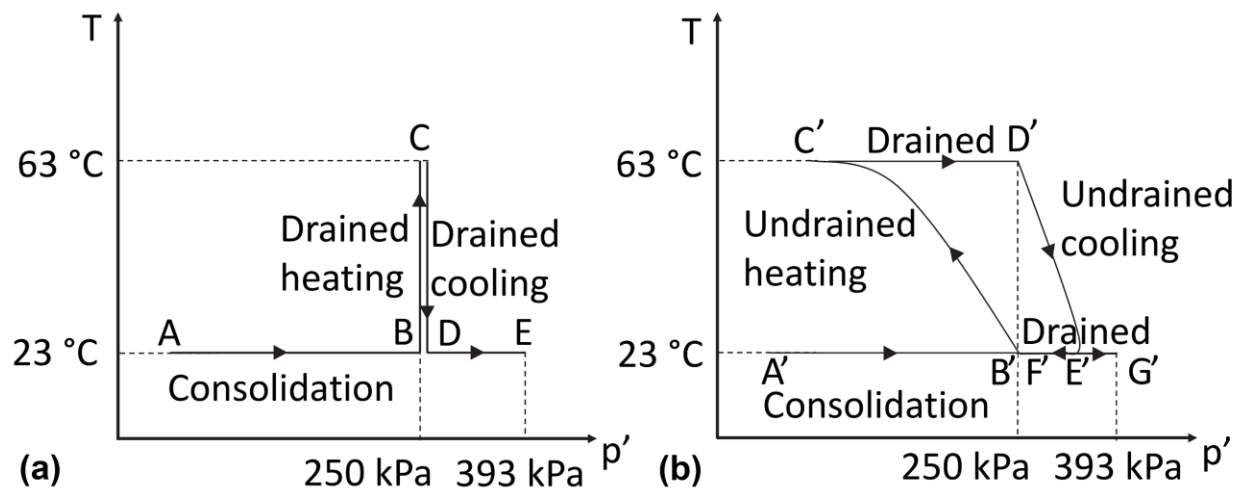
641

(b)

642 **Fig. 1.** Thermal triaxial system with bender elements: (a) Picture of assembled cell prior to  
 643 installation of insulation around the cell; (b) Schematic of the triaxial set-up showing the  
 644 internal instrumentation and the circulation system



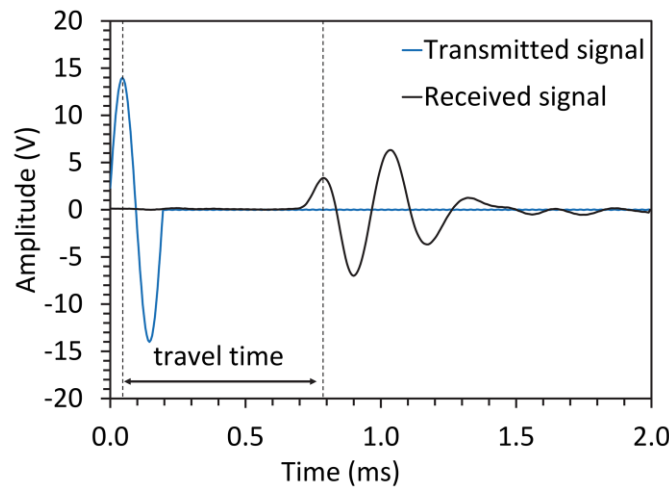
645

646 **Fig. 2.** Machine deflection of the thermal triaxial system

647

648 **Fig. 3.** Thermo-mechanical paths: (a) Drained heating-cooling cycle; (b) Undrained  
649 heating-cooling cycle with drainage after reaching thermal equilibrium in the heating and  
650 cooling stages

651

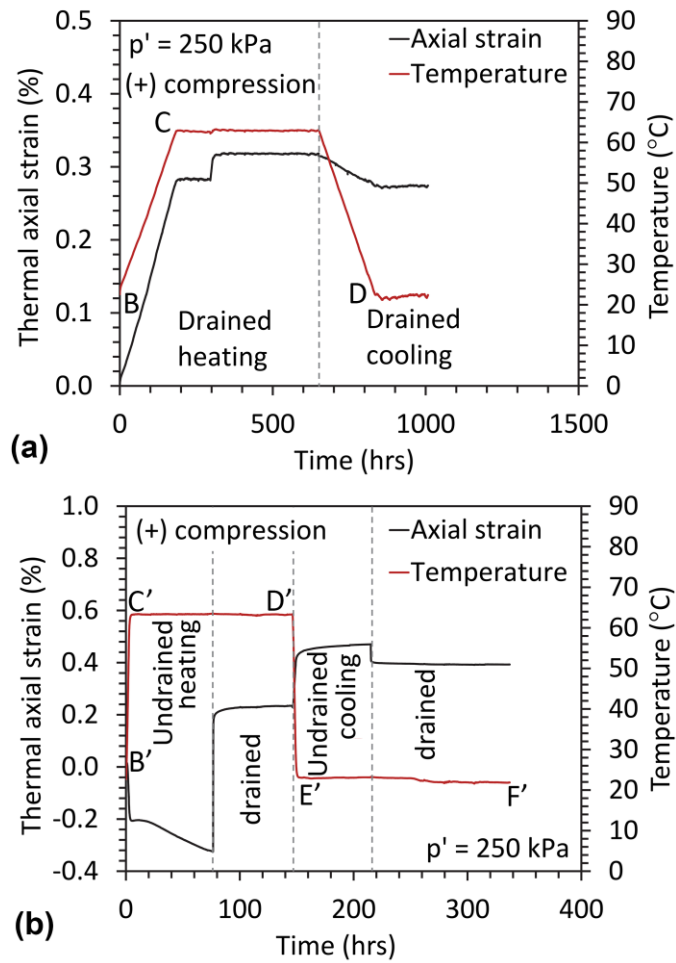


652

653 **Fig. 4.** Typical shear wave signals obtained from bender elements in a thermal triaxial cell

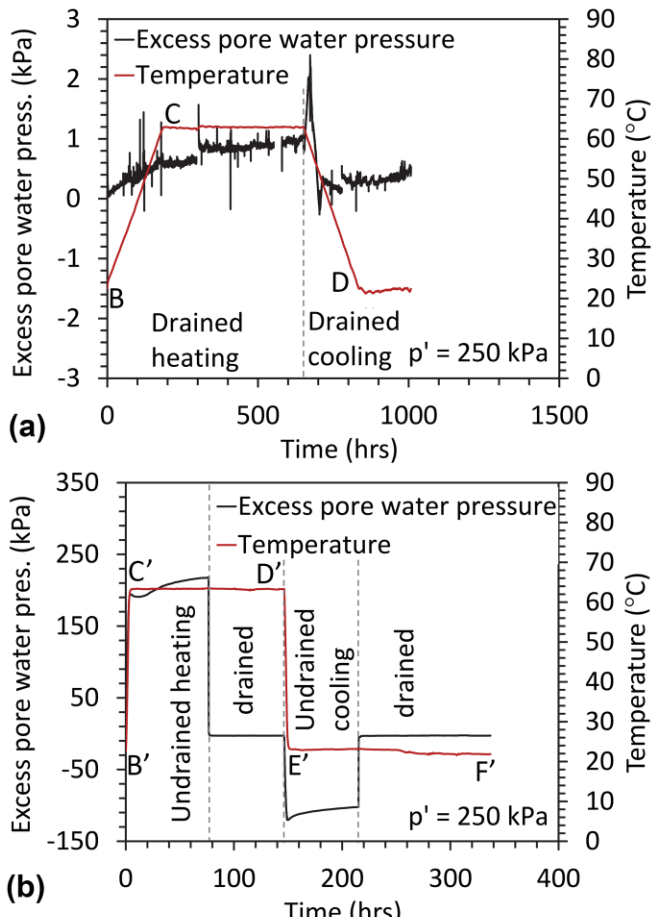
654

655



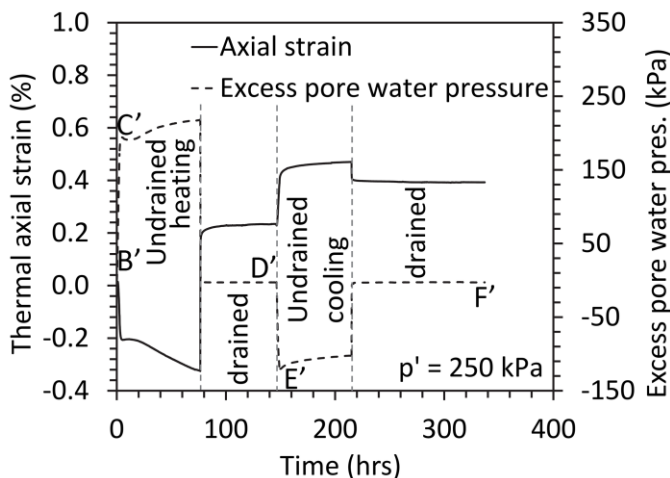
656

657 **Fig. 5.** Changes in axial strain during heating and cooling: (a) Drained heating-cooling cycle;  
 658 (b) Undrained heating-cooling cycle



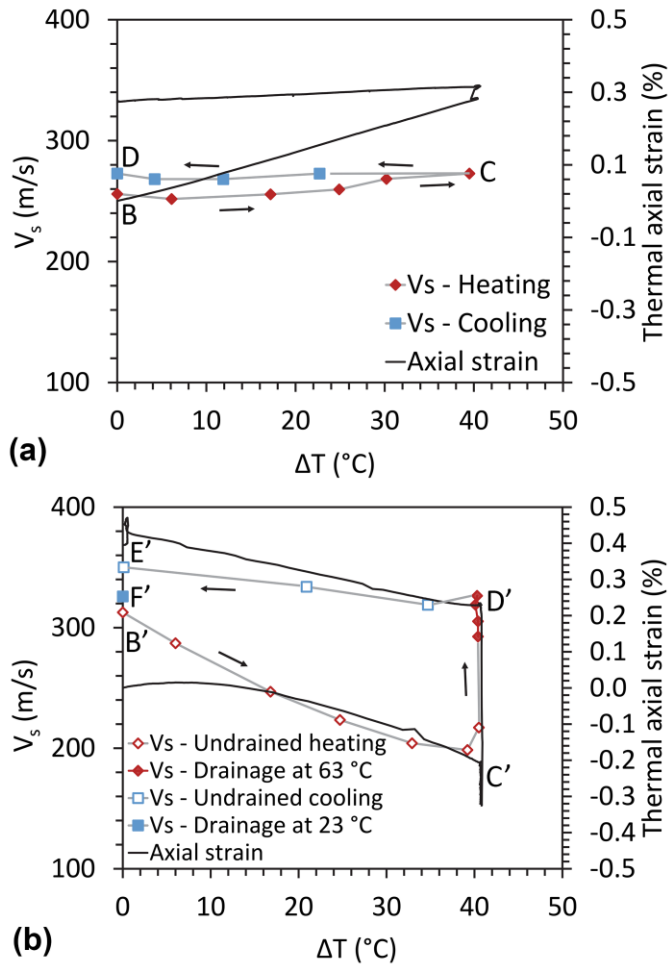
659

660 **Fig. 6.** Excess pore water pressure during heating and cooling: (a) Drained heating-cooling cycle;  
 661 (b) Undrained heating-cooling cycle



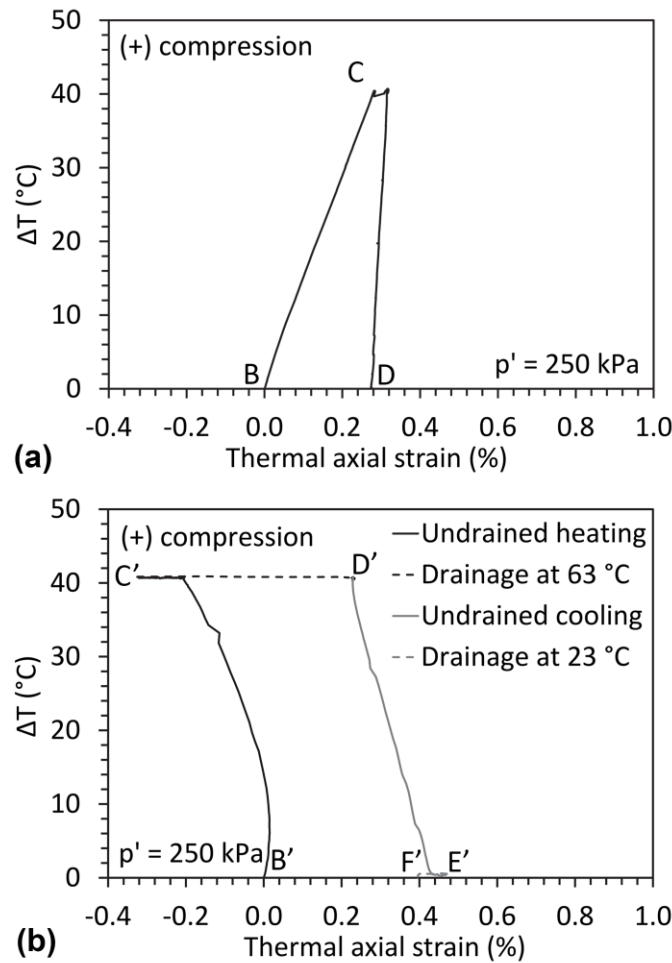
662

663 **Fig. 7.** Changes in thermal axial strain and excess pore water pressure with time



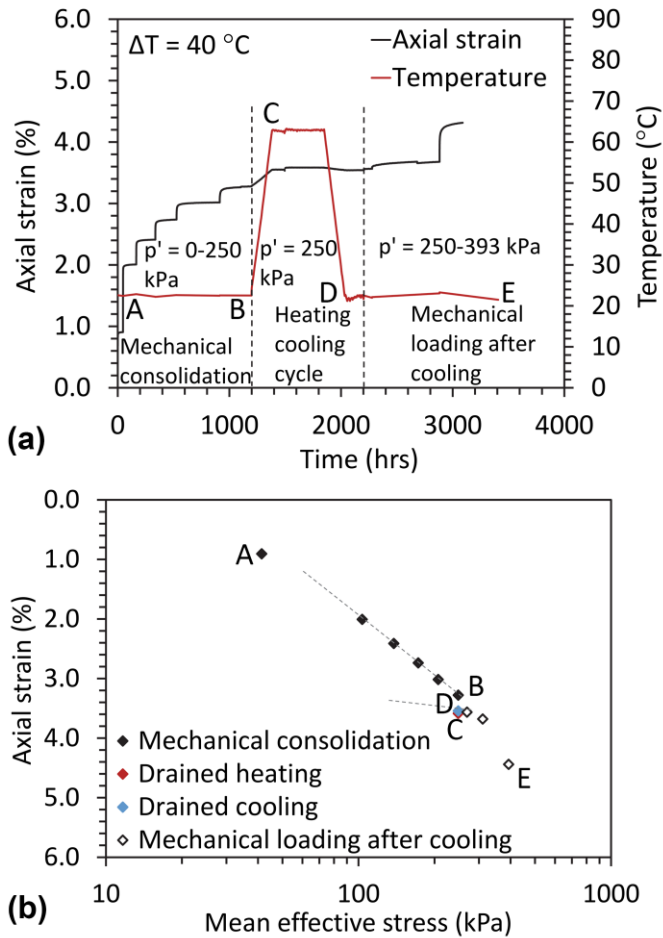
664

665 **Fig. 8.** Changes in shear wave velocity and thermal axial strain with temperature: (a) Drained  
 666 heating-cooling cycle; (b) Undrained heating-cooling cycle



667

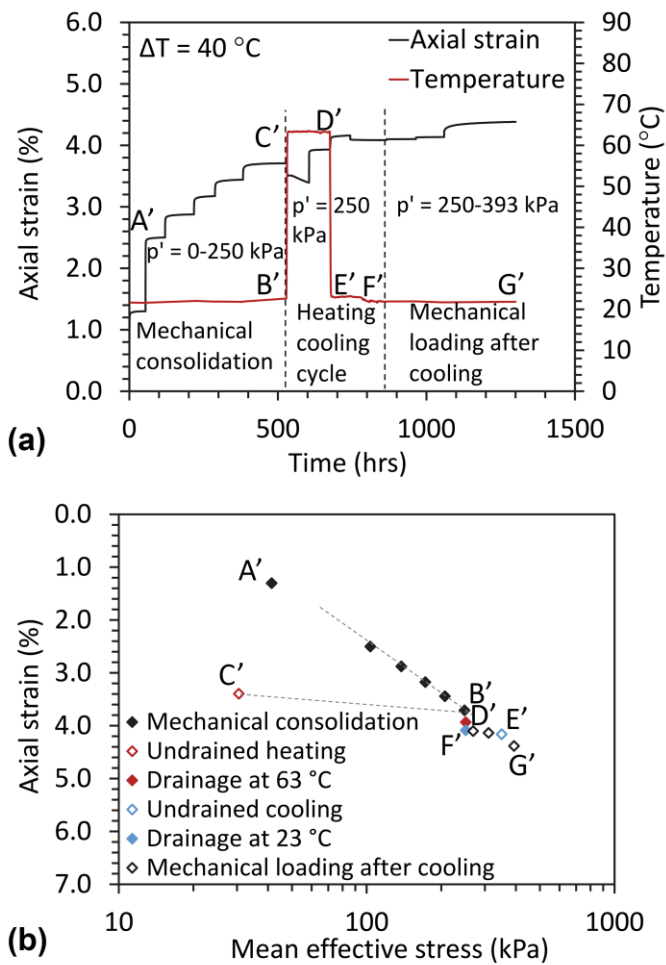
668 **Fig. 9.** Changes in thermal axial strain with temperature: (a) Drained heating-cooling cycle;  
 669 (b) Undrained heating-cooling cycle



670

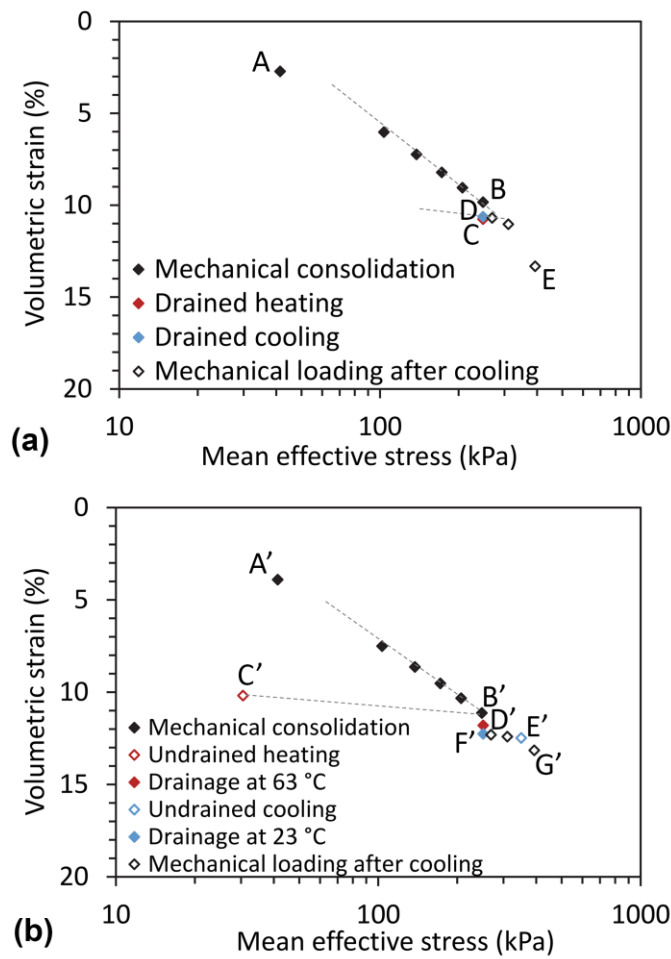
671 **Fig. 10.** Thermo-mechanical response of kaolinite subjected to a drained heating-cooling cycle:

672 (a) Change in axial strain with time; (b) Axial compression curve



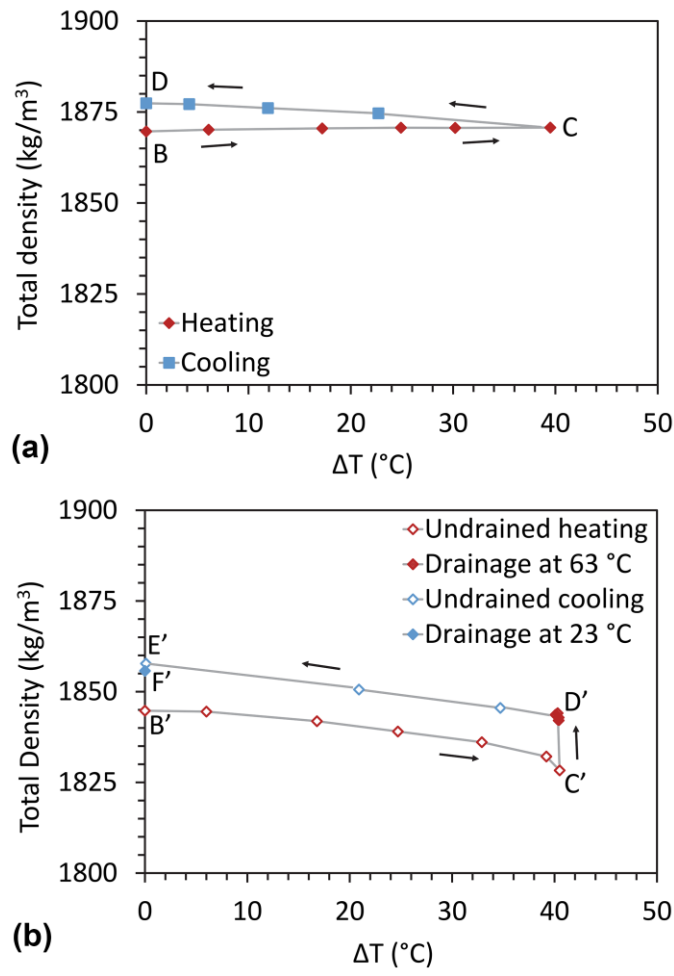
673

674 **Fig. 11.** Thermo-mechanical response of kaolinite subjected to an undrained heating  
 675 cooling cycle: (a) Change in axial strain with time; (b) Axial compression curve



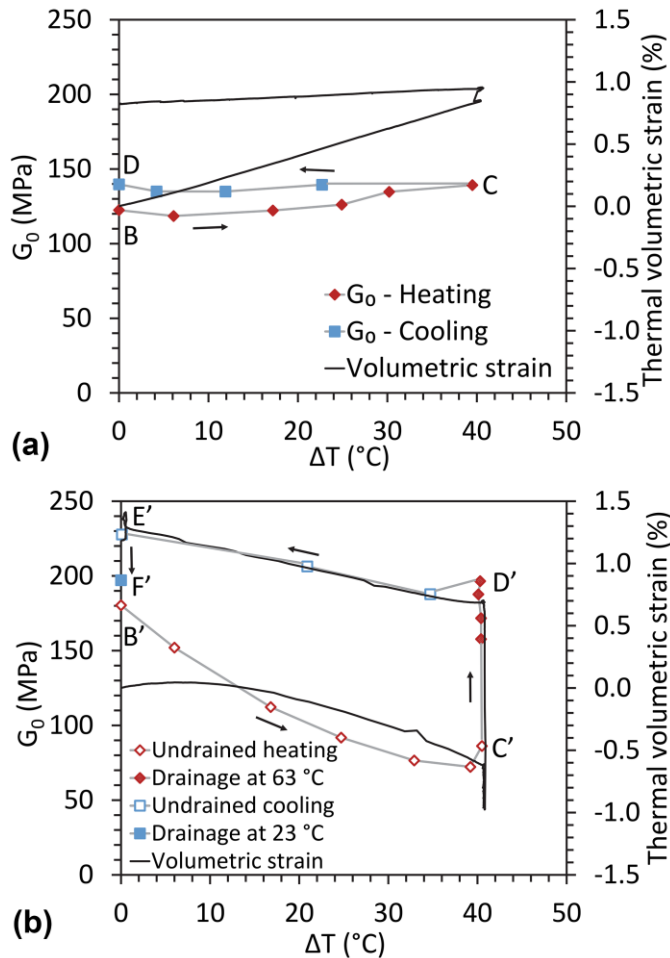
676

677 **Fig. 12.** Compression curves replotted in terms of volumetric strain: (a) Drained heating-cooling  
678 cycle; (b) Undrained heating-cooling cycle



679

680 **Fig. 13.** Changes in total density of the soil specimens with temperature: (a) Drained heating-  
 681 cooling cycle; (b) Undrained heating-cooling cycle



682

683 **Fig. 14.** Changes in small strain shear modulus and thermal volumetric strain with temperature:

684 (a) Drained heating-cooling cycle; (b) Undrained heating-cooling cycle